

Nanoscale

Accepted Manuscript

This article can be cited before page numbers have been issued, to do this please use: M. Shimizu, Y. Inami, R. Shimogawa, T. Matsuo, Y. Fujikata, H. Matsumoto, K. Mitsuishi and A. Hashimoto, *Nanoscale*, 2026, DOI: 10.1039/D5NR05414A.



This is an Accepted Manuscript, which has been through the Royal Society of Chemistry peer review process and has been accepted for publication.

Accepted Manuscripts are published online shortly after acceptance, before technical editing, formatting and proof reading. Using this free service, authors can make their results available to the community, in citable form, before we publish the edited article. We will replace this Accepted Manuscript with the edited and formatted Advance Article as soon as it is available.

You can find more information about Accepted Manuscripts in the [Information for Authors](#).

Please note that technical editing may introduce minor changes to the text and/or graphics, which may alter content. The journal's standard [Terms & Conditions](#) and the [Ethical guidelines](#) still apply. In no event shall the Royal Society of Chemistry be held responsible for any errors or omissions in this Accepted Manuscript or any consequences arising from the use of any information it contains.

ARTICLE

Atomic-Scale Elucidation of Formation and Structure in High-Performance Re-Ge NanocatalystsMasahiko Shimizu,^{*a,b,c} Yuta Inami,^a Ryuichi Shimogawa,^{a,d} Takeshi Matsuo,^a Yu Fujikata,^a Hajime Matsumoto,^{a,b} Kazutaka Mitsuishi^{*e} and Ayako Hashimoto^{*b,c}Received 00th January 20xx,
Accepted 00th January 20xx

DOI: 10.1039/x0xx00000x

Rational design of high-performance bimetallic nanocatalysts requires an understanding of the unique atomic structures governing their performance. This study focused on the Re-Ge/TiO₂ catalyst, which exhibits high performance for carboxylic acid hydrogenation. We analyzed structural and electronic-state changes during its multistep preparation involving calcination in air, hydrogen reduction, and oxidative stabilization, to elucidate structural factors responsible for the high performance. Therefore, we used complementary *in-situ* X-ray absorption fine structure analysis and *ex-situ* scanning transmission electron microscopy (STEM). The STEM imaging utilized an air-free transfer holder to track individual nanoparticles and address two issues: the challenge of distinguishing true structural changes from variations among different particles, and electron beam damage associated with long exposure times. It was revealed that the highly active state after hydrogen reduction originates from approximately 1-nm crystalline alloy nanoparticles. The nanoparticle structure was a unique, low-energy, face-centered cubic fragment, verified by density functional theory calculations. Furthermore, quantitative STEM analysis demonstrated that the nanoparticles were a random alloy of Re and Ge. This atomic-level mixing, as detected by the spatially averaged X-ray absorption, considered to stabilize the metallic state, resulting in electron-rich Re. These findings provide a new strategy for designing high-performance nanocatalysts and establishes the correlative methodology as a way to identifying performance-determining factors in complex nanomaterials.

Introduction

Bimetallic nanoparticles are critically important in the design of next-generation functional materials. They exhibit unique properties attributed to interactions between constituent elements.^{1,2} This strategy is particularly powerful for catalysis, where combinations of different elements can precisely control activity and selectivity at the atomic level via geometric and electronic effects.^{3,4} Rhenium (Re) is a crucial catalytic element exhibiting excellent activity in various hydrogenation reactions.^{5–10} To enhance its performance, functional optimization through combinations with other elements is essential. Indeed, alloying Re with elements such as Pd, Pt, Ru, Fe, and Ni has been reported to improve catalytic activity.^{11–15}

We recently developed a novel nanocatalyst by combining Re with germanium (Ge).^{16,17} It exhibits higher selectivity in direct hydrogenation of carboxylic acids compared with monometallic Re catalysts, and has high activity and selectivity

comparable with commercial Ru-Pt-Sn catalysts.¹⁸ Furthermore, its precious-metal-free composition and low-cost preparation make it a promising candidate for industrial applications. However, the atomic-level structural and electronic origins of this performance enhancement remain unknown. Understanding these factors is essential for further enhancements and for rational designs of next-generation nanomaterials. Achieving this goal is significantly challenging. It requires accurately tracking atomic-level structural changes throughout multistep thermal treatments during catalyst preparations, which is difficult with conventional methods. For example, *in-situ* X-ray techniques provide spatially averaged information under reaction conditions,^{18,19} but do not resolve local structures of individual active sites.^{20,21} Atomic resolution via scanning transmission electron microscopy (STEM) provides local structural analysis.^{22–26} However, because different samples are typically imaged for revealing structural changes associated with each preparation step, effects of sample inhomogeneity, such as variations in particle size and shape, cannot be avoided. Therefore, it is very difficult to distinguish whether observed structural differences arose from changes during the preparation, or were simply particle-to-particle variations. While *in-situ* STEM enables dynamic imaging, it can also exhibit electron beam damage during long exposure times.^{27,28}

We addressed these challenges via a complementary multi-scale approach. With *in-situ* X-ray absorption fine structure (XAFS) analyses, we tracked changes in spatially averaged

^a Science & Innovation Center, Mitsubishi Chemical Corporation, 1000 Kamoshidacho, Aoba-ku, Yokohama, Kanagawa, Japan.

^b Research Center for Energy and Environmental Materials, National Institute for Materials Science, 1-2-1 Sengen, Tsukuba, Ibaraki, Japan.

^c Graduate School of Science and Technology, University of Tsukuba, 1-2-1 Sengen, Tsukuba, Ibaraki, Japan.

^d Department of Materials Science and Chemical Engineering, Stony Brook University, Stony Brook, New York 11794, United States

^e Center for Basic Research on Materials, National Institute for Materials Science, 1-2-1 Sengen, Tsukuba, Ibaraki, Japan. Supplementary Information available. See DOI: 10.1039/x0xx00000x



chemical states over the entire sample. We then used *ex-situ* STEM with an air-free transfer holder to directly image the corresponding structural changes of individual nanoparticles at the atomic scale. This approach enabled us to elucidate changes in both structural and electronic states during each preparation step of Re-Ge catalysts, and to identify the key structural factors responsible for high performance. Unique crystalline nanoparticles approximately 1 nm in size were observed in the highly active state after hydrogen reduction. Furthermore, XAFS spectroscopic analyses indicated that alloy formation stabilized the metallic, electron-rich, Re(0) state. These results confirm the new strategy for designing high-performance nanocatalysts, and demonstrate a precise analytical methodology for the structural analysis of various complex nanomaterials.

Materials and methods

Sample preparation

The TiO₂-supported Re-Ge catalyst (Re-Ge/TiO₂) was prepared with a co-impregnation method that was previously reported.¹⁷ An aqueous solution of NH₄ReO₄ and GeO₂ impregnated the support; this was followed by drying and calcination in air at 300 °C. The nominal loadings of Re and Ge were 5 wt% and 3 wt%, respectively. A portion of this calcined powder was directly used for *in-situ* XAFS measurements and as the starting material for *ex-situ* STEM imaging. To analyze the reduced catalyst, another portion of the powder was exposed to H₂ at 500 °C. The reduced sample was then stored in an argon-filled glove box.

X-ray diffraction analysis

Powder X-ray diffraction (XRD) patterns of TiO₂ and the hydrogen-reduced Re-Ge/TiO₂ catalyst were recorded on a diffractometer (D8 Advance, Bruker AXS) using Cu K α radiation (40 kV, 40 mA). Data were collected over a 2 θ range of 15–90° with a step size of 0.02°. To prevent exposure to air during the measurement, the sample was sealed in a Si-based airtight holder filled with argon.

For the calcined and oxidized Re-Ge/TiO₂ catalysts, powder XRD patterns were re-measured on a diffractometer (Empyrean, Malvern Panalytical) using Cu K α radiation (45 kV, 40 mA) in reflection mode. Data were collected over a 2 θ range of 10–80° with a step size of 0.008°. Each sample was measured by four repeated scans.

In-situ XAFS measurement

XAFS measurements were performed at the BL-9C beamline of the Photon Factory at KEK (Tsukuba, Japan). Re L₃-edge (10535 eV) and Ge K-edge (11103 eV) spectra were collected in transmission mode. *In-situ* measurements used an electric furnace cell equipped with an automated gas mixing system. The Re-Ge/TiO₂ or Re/TiO₂ sample was loaded into the cell, and spectra were first recorded in air. The sample was then reduced under flowing H₂ as the temperature was increased from room temperature to 500 °C at 10°C/min. XAFS spectra were recorded continuously during the temperature ramp. After holding it at

500 °C, the sample was then cooled to 50 °C under H₂. The gas atmosphere was then switched sequentially from H₂ to N₂, 5% O₂/N₂, and 20% O₂/N₂ at 50 °C to investigate the oxidation behavior. For comparison, Re/TiO₂ (without Ge) was analyzed under identical conditions.

XAFS data processing was performed with the Larch software package.²⁹ Energy calibration was conducted using Re and Ge metal references, where the edge energy (E₀) was defined as the first zero-crossing point of the second derivative of the absorption spectrum. This was 10535 eV for the Re L₃ edge and 11103 eV for Ge K edge. Extended XAFS (EXAFS) fitting was performed in R-space with FEFF8.5L software bundled with Larch. Details of the fitting procedure are provided in the supporting information.

Ex-situ STEM observation

The calcined Re-Ge/TiO₂ catalyst powder was then loaded onto a microelectromechanical chip with a heating membrane (Hummingbird Scientific). To minimize background signals from the nitride (SiN_x) support membrane of the heating chip for high-resolution STEM imaging, multiple 2- μ m-diameter pores were created in the membrane with a gallium focused ion beam (JIB-4000, JEOL). The Re-Ge/TiO₂ powder was then loaded onto this chip, which was then mounted onto an air-free transfer TEM holder (Hummingbird Scientific). Prior to imaging, the sample surface was subjected to plasma cleaning (GV10x, Ibs group, inc.) to remove contaminants. All images were acquired with an aberration-corrected TEM (JEM-ARM200F, JEOL) operated at 200 kV. To minimize beam-induced changes, probe alignment (e.g., focusing) was performed in a different area from the observation target, and the target nanoparticles were exposed only during image acquisition. The probe current was kept at ~20 pA. For *ex-situ* processing, the sample mounted in the air-free holder was transferred from the TEM to a vacuum chamber. Inside the chamber, the sample was heated with the membrane chip under a sealed atmosphere of selected preparation gases at approximately 0.5 atm. The procedure consisted of hydrogen reduction (500 °C, 30-min hold), followed by oxidative stabilization (5% O₂/N₂ at room temperature). After each step, the holder was returned to the TEM without exposure to air, which allowed imaging of structural changes in the same nanoparticles. High-angle annular dark-field STEM (HAADF-STEM) images were acquired with a convergence angle of 20.8 mrad, a 2048 \times 2048 pixel image size, and a dwell time of 5 μ s per pixel.

High-resolution STEM observation of nanoparticles after hydrogen reduction

To analyze the composition and crystal structure of the nanoparticles in their high-performance state after hydrogen reduction, high-resolution STEM images were acquired. The hydrogen-reduced Re-Ge/TiO₂ powder was handled under an inert atmosphere to prevent exposure to air. Inside an argon-filled glovebox, the powder was dispersed onto a copper mesh (EM Japan) to prepare a TEM grid that was loaded onto an air-free transfer holder (JEOL) for insertion into an aberration-corrected TEM (JEM-ARM300F, JEOL). Imaging was performed



with an acceleration voltage of 300 kV. HAADF-STEM images were acquired with a convergence semi-angle of 23.6 mrad and a collection range of 73–175 mrad. The image size and dwell time were 2048 × 2048 pixels and 5 μs/pixel, respectively. For elemental mapping, STEM combined with energy dispersive X-ray spectroscopy (STEM-EDS) was performed separately with an acquisition time of 300 s.

Density-functional theory calculations

To examine possible stable Re nanocluster structures, we performed structural optimization calculations based on those reported previously.³⁰ Thirty different 55-atom clusters with high symmetry were used as initial structures. Their relative stabilities were evaluated by comparing their total energies after structural optimization. Density functional theory (DFT) calculations were performed with the Quantum ESPRESSO package³¹, with plane-wave basis sets and projected augmented-wave pseudopotentials.^{32,33} The energy cutoff of the plane-wave basis set was 51 Ry. The exchange-correlation functionals were treated within the generalized gradient approximation using the Perdew-Burke-Ernzerhof³⁴ form. The finite-size clusters were placed in a cubic supercell having an edge length of 25 Å, which was sufficiently large to avoid interactions between clusters in neighboring cells. To account for the large size of the unit cells, all simulations were restricted to the Γ point of the Brillouin zone. During the geometric optimization, the convergence threshold was 10^{-6} Ry for self-consistent electronic minimization, and all atoms were allowed to relax until the forces were below 10^{-3} Ry/Å.

HAADF-STEM image simulation

To determine the atomic mixing pattern within the nanoparticles, contrast simulations were performed to reproduce the experimental HAADF-STEM image. All atomic models were constructed based on the crystal structure consistent with the STEM images and DFT calculations. The models were initially created as spherical clusters, with diameters set to match the experimentally observed particle size, and their central coordinates were set to align with the arrangement of atomic columns in the experimental images. We then generated several atomic models for major mixing patterns, including core-shell, subcluster-segregated, ordered alloy and random alloy structures, as described previously.^{1,2} The overall composition of each model was Re-rich, in accordance with STEM-EDS analyses. Finally, the models were cut into hemispheres to match the observed particle shape. To reproduce the intensities of each atomic column in the experimental images (as determined by two-dimensional Gaussian fitting), the substitutional Re and Ge sites were optimized. The HAADF-STEM image simulations were performed with the multi-slice method in the abTEM code.³⁵ All optical parameters, including the accelerating voltage, convergence angle, and HAADF detector collection angles, were set to match the experimental conditions. Thermal vibrations were included via a frozen phonon model with 100 configurations.

Results and discussion

View Article Online

DOI: 10.1039/D5NR05414A

Electronic and local structure analyses of hydrogen reduction and oxidative stabilization

The standard preparation method for the Re-Ge catalyst consists of three sequential gas-phase treatments after the impregnation of Re and Ge precursors onto the TiO₂ support: (1) calcination in air to decompose supported salts, (2) hydrogen reduction for catalyst activation, and (3) oxidative stabilization to enable handling in air.¹⁷ While the Re-Ge catalyst prepared by hydrogen reduction (step 2) exhibits high hydrogenation activity and selectivity, the subsequent oxidative stabilization step (step 3) can decrease both catalytic activity and selectivity, despite being essential for safe handling at the industrial scale.³⁶ Understanding this deactivation mechanism by identifying and eliminating the primary cause of performance loss is crucial for improving catalyst manufacturing. To analyze the local structure and electronic state of the Re-Ge nanoparticles during these key processes, *in-situ* XAFS measurements were performed for both the reduction and oxidative stabilization steps.

Figure 1 shows XAFS spectra of Re-Ge/TiO₂ at different treatment stages, while Fig. S1 shows the temperature-dependent changes in X-ray absorption near edge structure (XANES) spectra during the reduction step. Fig. S2 presents XANES spectra from Fig. 2 overlaid with reference compounds: Re metal, ReO₂, ReO₃, and NH₄ReO₄ for the Re L₃ edge, and Ge(0) and hexagonal GeO₂ for the Ge K edge. Before reduction, the Re L₃ edge spectrum exhibited a peak position comparable with those of Re(IV), Re(VI), and Re(VII) references, confirming the presence of oxidized Re compounds (Fig. S2a). The corresponding Fourier transform spectrum (Fig. 2c) matches well with that of NH₄ReO₄ in R space. After hydrogen reduction at 500 °C, the white line intensity significantly decreases, and the edge position shifts to lower energy. However, it remains higher than that of Re(0), indicating partial reduction toward the metallic state (Fig. S2a). The Fourier transform spectrum shows that the intensity of the first coordination shell decreases as the reduction proceeds (Fig. 2c).

Similarly, for the Ge K edge, the XANES spectrum before reduction matches well with that of GeO₂, confirming that Ge exists in the Ge(IV) oxidized state (Fig. S2b). The Fourier transform spectrum (Fig. 2f) also shows good agreement with GeO₂ in R space. After hydrogen reduction, the edge position shifts to lower energy, and the intensity of the first-shell peak decreases. However, the white line intensity remains higher than that of Ge(0), indicating partial reduction, as observed for Re.

The temperature-dependent XANES spectra (Fig. S1) provided insight into the reduction mechanism. For the Re L₃ edge (Fig. S1a), the absence of an isosbestic point during reduction indicates that the transformation involved more than two chemical compounds. This suggests that the reduction of Re proceeded through multiple intermediate oxidation states, from Re(VII) and/or Re(VI) through Re(IV) to Re(0), rather than through a simple two-state conversion. Similar reductions of multiple intermediate species were also reported in the Re/TiO₂



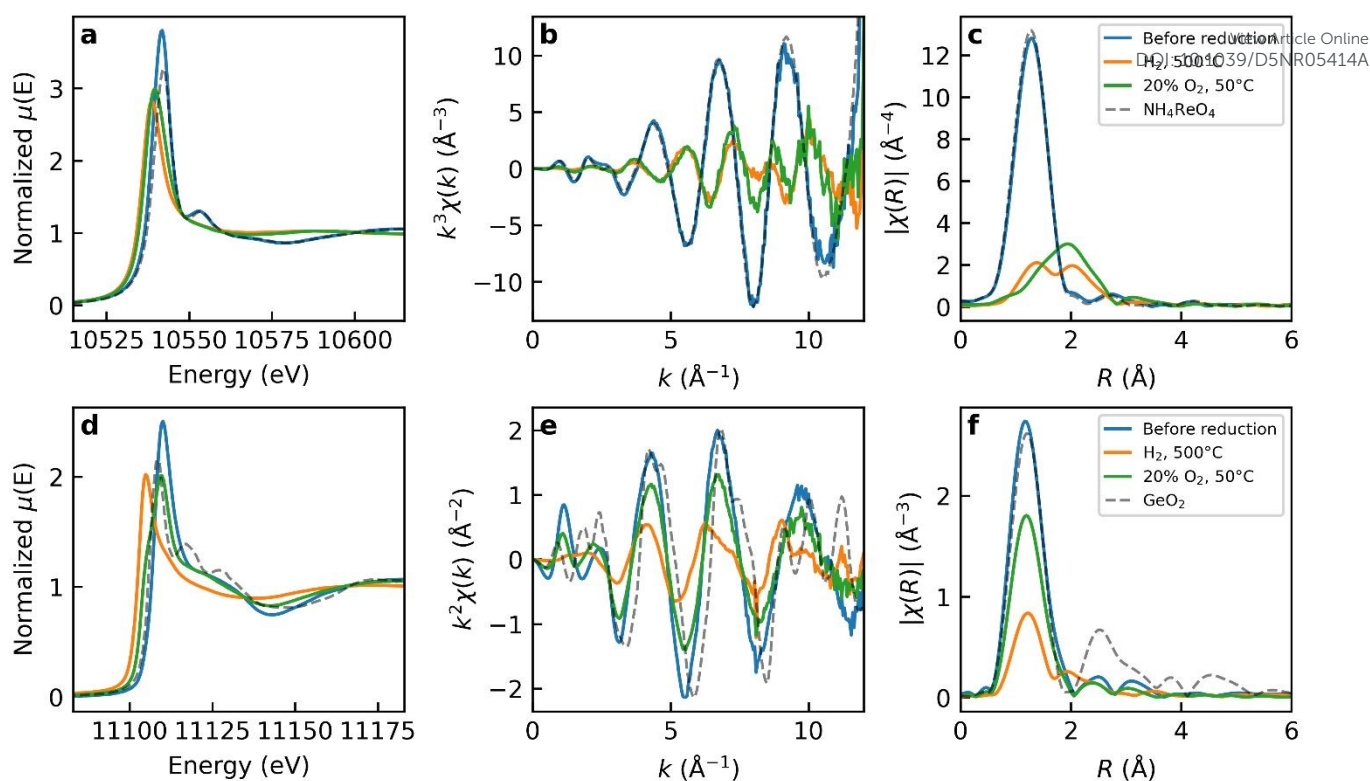


Fig. 2 X-ray absorption fine structure (XAFS) analysis of Re-Ge/TiO₂ at different treatment stages. Top row: Re L₃ edge data showing (a) X-ray absorption near edge structure (XANES), (b) k^3 -weighted extended XAFS (EXAFS) oscillations, and (c) Fourier transform magnitude. The NH₄ReO₄ reference is shown as a dashed line. Bottom row: Ge K edge data showing (d) XANES, (e) k^2 -weighted EXAFS oscillations, and (f) Fourier transform magnitude. The GeO₂ reference is shown as a dashed line. Data are shown for four conditions: before reduction (blue), after H₂ reduction at 500 °C (orange), and after exposure to 20% O₂ at 50 °C (green).

system.¹⁰ In contrast, the Ge K edge spectra (Fig. S1b) exhibit behavior consistent with a two-component system, suggesting that the reduction of Ge proceeded directly from Ge(IV) to Ge(0) without detectable intermediate oxidation states.

To quantitatively analyze the structural evolution during each step, EXAFS curve-fitting analyses were performed, as summarized in Table 1 and Table 2. Figure 2, Table S2, and Table S3 show the temperature dependences of the structural and fitting parameters during reduction. The individual fitting results in R-space are presented in Figs. S3-S5.

A significant difference was observed in the EXAFS spectra in R-space for Re-Ge/TiO₂ and Re/TiO₂ at 500 °C under H₂ (Fig. 3b), indicating the presence of Re-Ge bonds in the bimetallic catalyst. A two-shell fit with Re-O and Re-Ge paths reproduced the EXAFS signals, yielding a Re-Ge bond distance of 2.448 ± 0.066 Å, which is significantly shorter than the Re-Re bond distance reported for Re/TiO₂¹⁰ (2.76 ± 0.01 Å). A two-shell fit with Re-O and Re-Re paths did not adequately reproduce the experimental data owing to the longer bond distance of the Re-Re shell.

For the Re L₃ edge (Fig. 1a,b), the Re-O coordination number, N(Re-O), and Re-O bond distance, R(Re-O) (~1.7 Å) remain consistent with the tetrahedral ReO₄⁻ structure of NH₄ReO₄ below 280 °C. Above this temperature, N(Re-O) begins to decrease, indicating the onset of reduction. At intermediate temperatures (approximately 335 °C), EXAFS fitting required both short and long Re-O paths (Fig. S4I, Table S2), indicating the coexistence of multiple Re-O coordination environments consistent with the multi-step reduction suggested by XANES

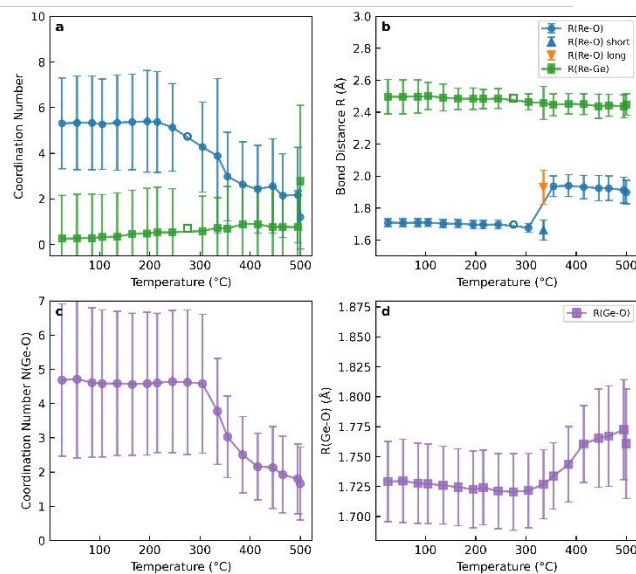


Fig. 1 Temperature dependence of extended X-ray absorption fine structure fitting parameters for Re-Ge/TiO₂ during H₂ reduction. (a) Coordination numbers from Re L₃ edge fitting: N(Re-O) (blue circles) and N(Re-Ge) (green squares). (b) Bond distances from Re L₃ edge fitting: R(Re-O) (blue circles) and R(Re-Ge) (green squares). (c) Coordination number N(Ge-O) from Ge K edge fitting. (d) Bond distance R(Ge-O) from Ge K edge fitting. The transition at ~335 °C corresponds to the onset of reduction and Re-Ge alloy formation. The 500 °C data point is from merged spectra to improve signal-to-noise ratio.

data. Above 335 °C, the model with a long Re-O bond provided physically reasonable parameters.



Table 1 Re L₃ edge extended X-ray absorption fine structure fitting results for Re-Ge/TiO₂ samples

View Article Online

DOI: 10.1039/D5NR05414A

Sample	Path	N	R (Å)	σ^2 ($\times 10^{-3}$ Å ²)	ΔE_0 (eV)	R-factor	χ^2_{ν}
Re-Ge/TiO ₂ before reduction	Re-O	5.3±2.7	1.775±0.032	0.0±1.9	7.5±8.3	2.9%	557.0
Re-Ge/TiO ₂ H ₂ 500°C	Re-O	1.2±1.4	1.899±0.074	0.1±11.9	-11.0±12.3	4.9%	135.1
	Re-Ge	2.8±3.3	2.448±0.066	10.7±8.8			
Re-Ge/TiO ₂ O ₂ 50°C	Re-O	1.3±1.4	2.067±0.055	0.1±5.0	14.6±10.0	5.4%	81.7
	Re-Ge	1.8±2.3	2.554±0.051	6.0±10.3			

Table 2 Ge K edge extended X-ray absorption fine structure fitting results for Re-Ge/TiO₂ samples

Sample	Path	N	R (Å)	σ^2 ($\times 10^{-3}$ Å ²)	ΔE_0 (eV)	R-factor	χ^2_{ν}
Re-Ge/TiO ₂ before reduction	Ge-O	4.7±2.2	1.729±0.034	0.0±5.1	-1.0±7.2	5.0%	1092.0
Re-Ge/TiO ₂ H ₂ 500°C	Ge-O	1.5±0.4	1.735±0.018	0.0±3.6	-10.0±4.0	1.8%	29.8
	Ge-Re	3.0±2.1	2.547±0.029	12.7±7.0			
Re-Ge/TiO ₂ O ₂ 50°C	Ge-O	3.2±1.4	1.738±0.032	0.6±5.0	0.7±6.6	4.6%	881.3

Above 335 °C, N(Re-Ge) begins to increase as N(Re-O) continues to decrease, indicating the formation of Re-Ge bonds concurrent with the loss of Re-O coordination. However, owing to the large error bars associated with the Re-Ge coordination number, only a trend of increasing N(Re-Ge) can be inferred. However, owing to the strong correlation between the coordination number and the Debye-Waller factor (σ^2) in the EXAFS fitting, the error bars associated with N(Re-Ge) and σ^2 (Re-Ge) are too large to allow a quantitative comparison; therefore, only a trend of increasing N(Re-Ge) can be inferred. At 500 °C, the fitting results show N(Re-Ge) = 2.8 ± 3.3 with R(Re-Ge) = 2.448 ± 0.066 Å (Table 1).

For the Ge K edge (Fig. 2c,d), N(Ge-O) and R(Ge-O) (~1.73 Å) remain consistent with GeO₂ below 300 °C (Fig. S5). Above this temperature, N(Ge-O) decreases as does Re, suggesting concurrent reduction and alloy formation. It is noteworthy that even after 500 °C reduction under H₂, a significant Ge-O contribution remains with N(Ge-O) = 1.5 ± 0.4 (Table 2), indicating that a substantial fraction of Ge exists as oxides on the TiO₂ support.

For the spectrum at 500 °C, fitting with a two-shell model including Ge-O and Ge-Re paths yielded N(Ge-Re) = 3.0 ± 2.1 and R(Ge-Re) = 2.547 ± 0.029 Å (Table 2). This spectrum could also be fitted with a two-shell model including Ge-O and Ge-Ge paths, yielding N(Ge-Ge) = 1.2 ± 1.3 and R(Ge-Ge) = 2.431 ± 0.033 Å (Table S1). This Ge-Ge bond distance is comparable to that in Ge bulk (2.45 Å).³⁷ Although the Ge-Re model provided a

marginally better fit (R-factor = 1.8% vs. 3.3%), both structural models remain plausible given the similar fit quality, and the Ge K-edge data alone do not allow us to exclude Ge-Ge bonding. The fitted Ge-Re bond distance (2.547 Å) is slightly longer than the Re-Ge distance obtained from the Re L₃ edge analysis (2.448 Å). Nevertheless, these values are comparable within experimental uncertainty. Considering the clear Re-Ge contribution observed from the Re L₃ edge, we conclude that Ge-Re bonds are present in the reduced catalyst. However, the Ge-Ge contribution may also be significant, suggesting that both Ge-Re and Ge-Ge coordination environments coexist in the reduced catalyst.

The XANES spectra of Re-Ge/TiO₂ and Re/TiO₂ were compared to investigate the effect of Ge addition on the electronic state of Re. Fig. S6 shows the Re L₃ edge XAFS analysis of the Re/TiO₂ catalyst at different treatment stages, and Fig. 3 presents a direct comparison between Re-Ge/TiO₂ and Re/TiO₂. After hydrogen reduction at 500 °C, the Re L₃ edge XANES spectrum of Re-Ge/TiO₂ exhibits a lower white line intensity and a slight shift to lower energy compared with that of Re/TiO₂ (Fig. 3a). This decrease in white line intensity indicates that Re in the bimetallic catalyst has a higher electron density, suggesting that the formation of the Re-Ge alloy stabilizes the Re(0) state more effectively than in the monometallic catalyst. This electron-rich Re is closely related to the enhanced Re-Ge catalytic performance.

The structural changes were investigated to understand the origin of decreased catalytic performance after oxidative stabilization. Upon exposure to 20% O₂ at 50 °C, distinctly different behaviors were observed for Re-Ge/TiO₂ and Re/TiO₂ catalysts (Fig. 3). For Re/TiO₂, significant changes in both the XANES spectrum and the Fourier transform magnitude were observed after oxidation (Fig. S6), indicating substantial re-oxidation of Re(0). In contrast, Re-Ge/TiO₂ exhibited relatively minor changes in the Re L₃ edge spectra after oxidative stabilization (Fig. 2a-c), with the white line intensity remaining lower than that of Re/TiO₂ (Fig. 3a). This suggests that the Re-Ge alloy structure provides enhanced oxidation resistance when compared with Re/TiO₂.

The EXAFS fitting results (Table 1 and Table 2) also support this interpretation. For the Re L₃ edge, the Re-Ge bond remains

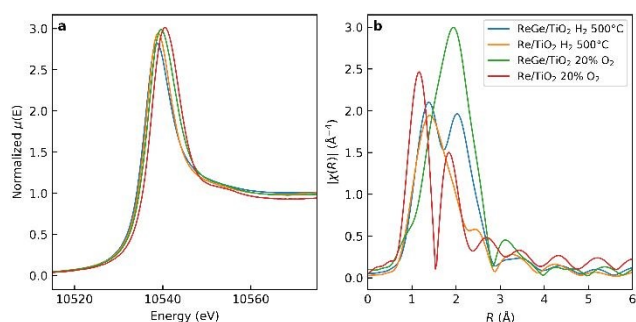


Fig. 3 Comparison of Re L₃ edge extended X-ray absorption fine structure for Re-Ge/TiO₂ and Re/TiO₂ catalysts. (a) X-ray absorption near edge structure spectra and (b) Fourier transform magnitude. Re-Ge/TiO₂ H₂ 500°C (blue), Re/TiO₂ H₂ 500°C (orange), Re-Ge/TiO₂ 20% O₂ (green), Re/TiO₂ 20% O₂ (red).



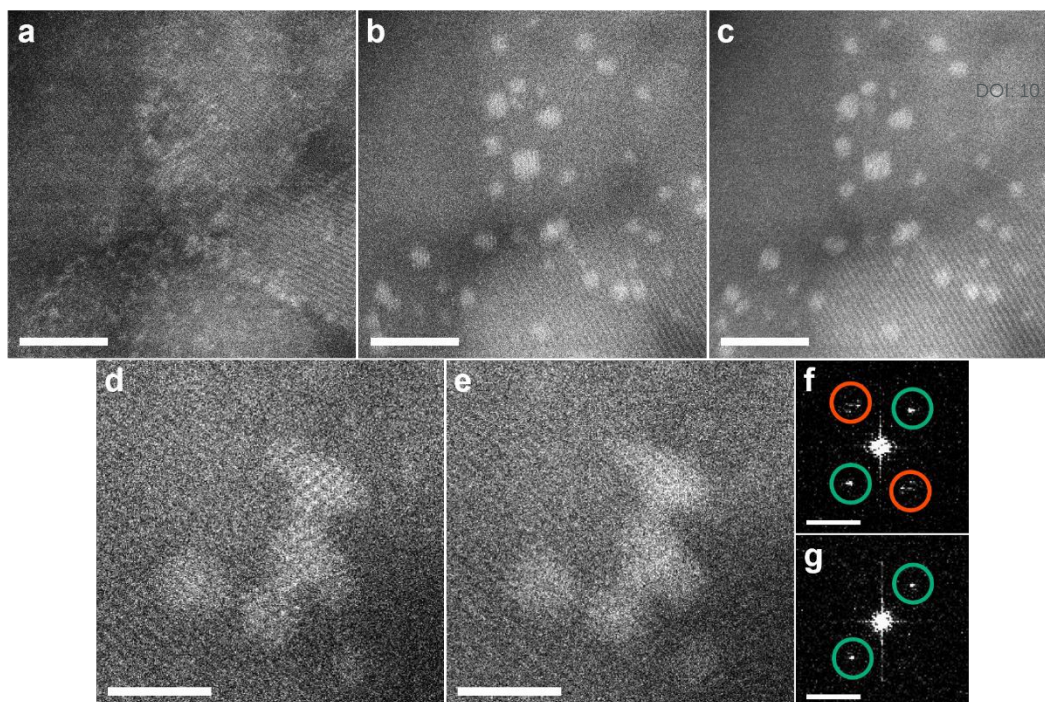
View Article Online
DOI: 10.1039/D5NR05414A

Fig. 4 *Ex-situ* High-angle annular dark-field scanning transmission electron microscopy images of the Re-Ge/TiO₂ catalyst at each preparation stage. (a-c) A series of images showing the same field of view after (a) calcination in air, (b) hydrogen reduction, and (c) oxidative stabilization. (d, e) High-magnification images of the same nanoparticle after (d) hydrogen reduction and (e) oxidative stabilization. (f, g) Corresponding fast Fourier transform patterns of the images shown in (d) and (e), respectively. The red and green circles indicate diffraction spots originating from the nanoparticle and the TiO₂ support, respectively. Note that the spots from the nanoparticle are absent in (g) after oxidative stabilization. Scale bars: 5 nm in (a-c); 2 nm in (d, e); 5 nm⁻¹ in (f, g).

detectable after oxidative stabilization with $N(\text{Re-Ge}) = 1.8 \pm 2.3$ and $R(\text{Re-Ge}) = 2.554 \pm 0.051 \text{ \AA}$ (Table 1). Although no definitive conclusion can be drawn regarding the coordination number owing to the strong $N\text{-}\sigma^2$ correlation in the fit, the persistence of the Re-Ge contribution suggests that the Re-Ge alloy structure formed at high temperature is at least partially preserved, indicating that the Re-Ge alloy layer has higher resistance to oxidation. In contrast, at the Ge K edge, the coordination number $N(\text{Ge-O})$ increases from 1.5 ± 0.4 (H₂, 500 °C) to 3.2 ± 1.4 (O₂, 50 °C) after oxidation (Table 2), while the second shell peak corresponding to Ge-Re (or Ge-Ge) bonds significantly decreases in intensity (Fig. 2f, comparing green and red curves). This indicates that the reduced Ge compounds have been substantially re-oxidized.

These observations suggest that the addition of Ge leads to the formation of a stable Re-Ge alloy layer that confers oxidation resistance, thereby stabilizing the Re(0) state. Meanwhile, most of the Ge exists as Ge-Ge-rich regions or oxide species on the support, and are readily converted to GeO₂ under oxidizing conditions. The re-oxidation of Ge compounds within the alloy nanoparticles upon oxidative stabilization is expected to disrupt the atomic-level mixing of Re and Ge that characterizes the active state. This would potentially lead to structural degradation of the nanoparticles.

Observation of structural changes during catalyst preparation stages

To elucidate the structural changes corresponding to chemical state changes detected with *in-situ* XAFS, further analyses were performed. First, XRD measurements were conducted on the catalyst at various treatment stages, including after calcination,

after hydrogen reduction, and after subsequent oxidation (Fig. S7). In all cases, only diffraction peaks originating from the TiO₂ support (anatase) were observed, and no crystalline phases of Re, Ge, or their alloys were detected. Therefore, we performed *ex-situ* STEM imaging to track the structural changes at each preparation step at the atomic scale. The environmental conditions of the catalyst preparation (calcination in air, hydrogen reduction, and oxidative stabilization) were reproduced in the air-free transfer TEM holder and the vacuum chamber. This enabled us to track the same individual nanoparticles without exposing the sample to ambient air.

Figure 4a-c shows *ex-situ* HAADF-STEM images of the same field of view at each preparation step. After calcination in air (Fig. 4a), both Re and Ge species were found to be highly dispersed on the TiO₂ support, primarily as sub-nanoscale clusters and some individual atoms. In contrast, nanoparticles were formed after subsequent hydrogen reduction (Fig. 4b). The particle size distribution of approximately 700 particles, according to a reported method,³⁸ yielded an average diameter of $1.3 \pm 0.3 \text{ nm}$ (see histogram in Fig. S8). The nanoparticles remain visible after the final oxidative stabilization step (Fig. 4c), with no observable changes in size or position. These observations directly demonstrate that approximately 1-nm nanoparticles are formed from dispersed atoms during hydrogen reduction. Furthermore, their size and position on the support remain unchanged at the atomic level during oxidation stabilization. Figure 4d,e shows HAADF-STEM images of the same particle after hydrogen reduction and after oxidation stabilization, respectively. Highly active particles after hydrogen reduction exhibit lattice fringes. In contrast, the fringes disappear for low-activity particles after oxidation stabilization.



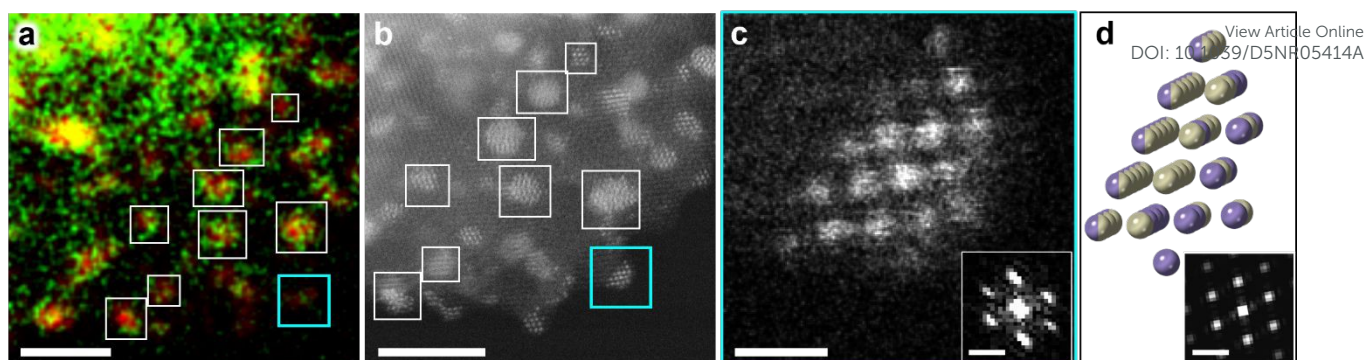


Fig. 5 Scanning transmission electron microscopy (STEM) analysis of nanoparticles after hydrogen reduction (a) STEM energy dispersive X-ray spectroscopy elemental map. Two maps, Re M (red) and Ge L (green), are superimposed. Representative particles are indicated by frames. (b) High-angle annular dark-field STEM (HAADF-STEM) image of an area nearly identical to (a). (c) Magnified HAADF-STEM image of the particle outlined in sky-blue in (a, b) and its corresponding fast Fourier transform pattern (inset). (d) Atomic model based on the face-centered cubic fragment structure obtained from density functional theory calculations and a simulated diffraction pattern (inset). The model is shown slightly tilted from the zone-axis orientation for clarity. Atom colors indicate Re (beige) and Ge (purple). Atoms whose elemental assignment was unclear owing to overlap with the support are displayed in two colors. Scale bars: (a, b) 5 nm; (c) 0.5 nm; inset in (c, d) 5 nm⁻¹.

This loss of crystallinity was also confirmed by the disappearance of diffraction spots originating from the nanoparticles in the corresponding fast Fourier transform (FFT) images (Fig. 4f-g, Fig. S9). Under our imaging conditions, control irradiation experiments confirmed that these crystallization/amorphization changes were not beam-induced but originated from the respective treatments (Fig. S10).

The Re-Ge/TiO₂ catalytic performance differs between the post-hydrogen-reduction state (high activity and selectivity) and the post-oxidation-stabilization state (low activity and selectivity).³⁶ Results from Fig. 4b-c indicate that this performance decline cannot be explained by changes in particle size or dispersion. Therefore, the loss of nanoparticle crystallinity, revealed in Fig. 4d-g, may be the direct cause of deactivation. This is consistent with the *in-situ* XAFS results, which showed that Ge in the nanoparticles was re-oxidized upon exposure to oxygen, as evidenced by increased Ge-O coordination and decreasing Ge-Re contributions. The Ge oxidation disrupts the atomic-level Re-Ge mixing essential for stabilizing the Re(0) state, thereby explaining both the observed loss of crystallinity and the accompanying decline in catalytic performance. Thus, the ability to clearly decouple multiple structural factors that can affect performance was attributed to the complementary approach that combined spatially averaged XAFS chemical state information with direct STEM structural imaging.

Atomic-scale structural analysis of nanoparticles in the active state

We then analyzed the atomic structure of the nanoparticles in their active state after hydrogen reduction. Re is considered to be the primary active site, while Ge functions as a co-catalyst that enhances selectivity.^{16,36} If the stabilization of the Re(0) state by Re-Ge alloy formation suggested by *in-situ* XAFS is key to the co-catalyst effect, elucidating the atomic arrangement within the nanoparticles is crucial. Therefore, we performed a detailed analysis of the composition, crystal structures, and atomic mixing patterns of the nanoparticles in their active state.

First, the composition of the nanoparticles was investigated using STEM-EDS. Figure 5a shows an elemental map superimposing Re M (red) and Ge L (green) maps (the individual

maps for Re and Ge are shown in Fig. S11). The nanoparticles contain Re and Ge, as shown for the representative particles highlighted by the frames. A quantitative analysis that was performed on approximately 50 particles indicated that both Re and Ge were detected in all particles, with an average Ge/Re atomic ratio of 0.53 ± 0.25 (see histogram in Fig. S12). This is consistent with the overall ratio of 0.51 obtained from the entire mapped area. The observed Ge/Re ratio is significantly lower than the nominal loading ratio of approximately 1.5, indicating that only a fraction of the loaded Ge is incorporated into the nanoparticle alloys. The remaining Ge most likely exists as highly dispersed GeO_x compounds on the TiO₂ support that are below the STEM-EDS detection limit. This interpretation is consistent with the substantial Ge-O coordination detected by XAFS after hydrogen reduction. This Re-rich composition, combined with the finding from *in-situ* XAFS that both elements are in metallic states, indicates that the particles are Re-based Re-Ge alloys. The formation of this Re-rich alloy is inconsistent with the bulk equilibrium phase diagram, where only the Ge-rich intermediate phase is considered stable.^{39,40} Therefore, the particles exist in a nanoscale-specific metastable phase.¹

The crystal structure of the nanoparticles was analyzed based on HAADF-STEM images. Figure 5b shows an image acquired from an area nearly identical to that in Fig. 5a, while Fig. 5c is a magnified image of a representative nanoparticle selected for analysis. This particle reflects the average characteristics of the nanoparticle population in terms of size (1.5-nm diameter) and composition (Ge/Re = 0.47). The FFT pattern obtained from the image of this particle (Fig. 5c, inset) shows hexagonal reflections. This characteristic structure was observed frequently for this catalyst (Fig. S13). However, the FFT pattern did not match the hexagonal close-packed (HCP) structure of bulk Re,⁴¹ the diamond structure of Ge,⁴¹ or the theoretically calculated icosahedron structure of Re nanoparticles.³⁰ Based on EDS analysis indicating this particle is Re-rich, we focused on Re-based structural models and first tested whether a distorted HCP Re structure could explain the experimental FFT. We therefore examined anisotropically distorted HCP Re models by varying the a-axis strain (ϵ_a) and c-axis strain (ϵ_c); however, none of them could reproduce the



experimental FFT patterns or the real-space atomic arrangement (Table S4 and Fig. S14). To explore alternative Re-based structural models that could explain the experimental results, we performed DFT calculations. The result revealed that, in addition to the previously reported icosahedron structure,³⁰ the face-centered cubic fragment (FCCf) structure^{30,42} was identified as a low-energy candidate (Fig. S15). Therefore, a hemispherical atomic model based on this FCCf structure was constructed, reflecting the experimentally observed particle size. Figure 5d shows the model and its corresponding simulated diffraction. This model showed good agreement with the experimental results (Fig. 5c) in both the real-space atomic arrangement (HAADF-STEM image) and the FFT reciprocal-space diffraction pattern. It should be noted that the present DFT calculations were performed for free-standing Re clusters without explicitly considering the TiO₂ support. Although support interactions may affect cluster stability and structure, such an analysis is beyond the scope of this study.

To elucidate the mixing pattern of Re and Ge atoms within this FCCf structure, we quantitatively analyzed the Z-contrasts in the HAADF-STEM images.^{43–45} The experimental intensity profiles were compared with simulated profiles based on major atomic ordering models for bimetallic nanoparticles, including core-shell, subcluster-segregated, ordered alloy and random alloy structures^{1,2} (see Fig. S16). The results showed that the random alloy model with Re and Ge mixed at the atomic level, as depicted in Fig. 5d, best reproduced the experimental image. This was consistent with the spatially averaged information from *in-situ* XAFS, indicating that Re and Ge coexisted within the first coordination spheres of each other. These results directly demonstrate, through both spectroscopic analyses and atomically resolved imaging, that the individual Re-Ge nanoparticles are random alloys with a unique FCCf crystal structure. Although the results of this study do not allow us to clearly distinguish the respective contributions of electronic effects (the electron-rich Re(0) state) and geometric effects (the shortened bond distances, the FCCf structure and random alloy character), both are likely to contribute to the catalytic activity.

Conclusions

This study focused on Re-Ge catalysts, which exhibit excellent activity and selectivity for the direct hydrogenation of carboxylic acids. Our aim was to elucidate the structural and electronic state changes during the preparation steps, and thereby identify the structural factors responsible for the high performance. A complementary approach combining *in-situ* XAFS and *ex-situ* STEM was thus used. The results revealed that the highly active state originates from approximately 1-nm crystalline nanoparticles formed during the hydrogen reduction step. The unique crystal structure of the nanoparticles was identified as low-energy FCCf, based on DFT calculations. Furthermore, Re and Ge mixed at the atomic level to form a random alloy in the particles. This stabilized the metallic Re(0) state, resulting in an electron-rich character of Re. Although the present results do not allow us to clearly distinguish the respective contributions of electronic and geometric effects,

both are likely to contribute to the high catalytic performance. We also found that the performance degradation accompanying the oxidative stabilization step was not because of changes in particle size or dispersion, but rather to re-oxidation of Ge within the nanoparticles, as revealed by increased Ge-O coordination in XAFS and the consequent loss of crystallinity observed with STEM. This correlation between changes in chemical state and physical structure highlights the critical importance of preserving the reduced Re-Ge alloy phase for maintaining high catalytic performance. This study elucidated the high-performance mechanism and demonstrated the importance of stabilizing unique metastable phases specific to the nanoscale and the resulting electronic interactions between elements. For the rational design of catalytic functions, the approach of directly linking spatially-averaged chemical state changes with the physical structural changes of individual nanoparticles was shown to be an effective way to identify performance-determining factors in complex nanomaterial systems.

Author contributions

M.S., R.S., Y.I. and T.M. proposed the project and designed the experiments. R.S., Y.I., and T.M. developed the Re-Ge/TiO₂ catalyst. Y.I. collected the *in-situ* XAFS data, and R.S. was responsible for the in-depth the XAFS/EXAFS data analysis and interpretation. M.S. performed the *ex-situ* and HAADF-STEM observations, quantitative STEM analysis, and related software-based image analysis. Y.F. conducted the DFT calculations and contributed to structural model visualization. T.M., R.S., and H.M. acquired funding and provided resources. K.M. and A.H. supervised the project and managed project administration. M.S. and R.S. co-wrote the manuscript and co-led the manuscript revision and response to reviewers, with contributions from all authors.

Conflicts of interest

There are no conflicts to declare.

Data availability

The data supporting this article have been included as part of the Supplementary Information. Supplementary information includes figures and tables for material characterization.

Acknowledgements

We thank Mr. Y. Kikuchi (MCC) and Mr. H. Yamanaka (MCC) for performing the XRD measurements and Dr. K. Okamoto (MCC) for their valuable support with the *in-situ* XAFS measurements, and Prof. Anatoly Frenkel (SBU) and Dr. Ramsey Salcedo (GC, CUNY) for providing reference spectra for the XAFS analysis. This study was partially supported by the "Advanced Research Infrastructure for Materials and Nanotechnology in Japan (ARIM)" department of the Ministry of Education, Culture,



Sports, Science, and Technology (MEXT) (Grant Number JPMXP1224NM5123), by KAKENHI, Japan Society for the Promotion of Science (Grant Number 24K15598, K.M.) and by Precursory Research for Embryonic Science and Technology (PRESTO), JST (Grant Number JPMJPR17S7, A.H.). We thank Edanz (<https://jp.edanz.com/ac>) for editing a draft of this manuscript.

References

- R. Ferrando, J. Jellinek and R. L. Johnston, *Chem. Rev.*, 2008, **108**, 845–910.
- K. D. Gilroy, A. Ruditskiy, H.-C. Peng, D. Qin and Y. Xia, *Chem. Rev.*, 2016, **116**, 10414–10472.
- D. Wang, H. L. Xin, R. Hovden, H. Wang, Y. Yu, D. A. Muller, F. J. DiSalvo and H. D. Abruña, *Nature Mater*, 2013, **12**, 81–87.
- V. R. Stamenkovic, B. S. Mun, M. Arenz, K. J. J. Mayrhofer, C. A. Lucas, G. Wang, P. N. Ross and N. M. Markovic, *Nature Mater*, 2007, **6**, 241–247.
- M. L. Gothe, K. L. C. Silva, A. L. Figueredo, J. L. Fiorio, J. Rozendo, B. Manduca, V. Simizu, R. S. Freire, M. A. S. Garcia and P. Vidinha, *European Journal of Inorganic Chemistry*, 2021, **2021**, 4043–4065.
- J. S. Reinhold, J. Pang, B. Zhang, F. E. Kühn and T. Zhang, *Green Chem.*, 2024, **26**, 10661–10686.
- J. Luo and C. Liang, *ACS Catal.*, 2024, **14**, 7032–7049.
- B. Rozmysłowicz, A. Kirilin, A. Aho, H. Manyar, C. Hardacre, J. Wärnå, T. Salmi and D. Yu. Murzin, *Journal of Catalysis*, 2015, **328**, 197–207.
- T. Toyao, S. M. A. H. Siddiki, A. S. Touchy, W. Onodera, K. Kon, Y. Morita, T. Kamachi, K. Yoshizawa and K. Shimizu, *Chemistry – A European Journal*, 2017, **23**, 1001–1006.
- M. L. Gothe, A. H. Braga, L. R. Borges, J. Hong, G. Farias, A. D. Torrez Baptista, B. A. L. Larico, A. B. M. Cansian, C. Rodrigues Miranda, S. R. Bare, L. M. Rossi and P. Vidinha, *ACS Catal.*, 2025, 19111–19126.
- Y. Takeda, M. Tamura, Y. Nakagawa, K. Okumura and K. Tomishige, *ACS Catal.*, 2015, **5**, 7034–7047.
- K. H. Kang, U. G. Hong, Y. Bang, J. H. Choi, J. K. Kim, J. K. Lee, S. J. Han and I. K. Song, *Applied Catalysis A: General*, 2015, **490**, 153–162.
- X. Cao, J. Zhao, F. Long, P. Liu, X. Jiang, X. Zhang, J. Xu and J. Jiang, *Applied Catalysis B: Environmental*, 2022, **312**, 121437.
- A. Suknev, V. Zaikovskii, V. Kaichev, E. Paukshtis, E. Sadovskaya and B. Bal'zhinimaev, *Journal of Energy Chemistry*, 2015, **24**, 646–654.
- X. Huang, K. Liu, W. L. Vrijburg, X. Ouyang, A. Iulian Dugulan, Y. Liu, M. W. G. M. Tiny Verhoeven, N. A. Kosinov, E. A. Pidko and E. J. M. Hensen, *Applied Catalysis B: Environmental*, 2020, **278**, 119314.
- Y. Inami, T. Matsuo, R. Shimogawa and T. Aoshima, *The 9th Tokyo Conference on Advanced Catalytic Science and Technology (TOCAT9)*, Fukuoka, Japan.
- Y. Inami, R. Shimogawa, T. Matsuo and M. Shimizu, Mitsubishi Chemical corporation Pat. P2025-133481A, 2025.
- Y.-L. Sun, Y.-L. Deng, H.-N. Chen, X.-T. Yang, X.-M. Lin and J.-F. Li, *Small Structures*, 2023, **4**, 2200201. DOI: 10.1039/D5NR05414A
- E. Groppo, S. Rojas-Buzo and S. Bordiga, *Chem. Rev.*, 2023, **123**, 12135–12169.
- A. A. Herzing, C. J. Kiely, A. F. Carley, P. Landon and G. J. Hutchings, *Science*, 2008, **321**, 1331–1335.
- E. I. Ross-Medgaarden, W. V. Knowles, T. Kim, M. S. Wong, W. Zhou, C. J. Kiely and I. E. Wachs, *J. Catal.*, 2008, **256**, 108–125.
- D. S. Su, B. Zhang and R. Schlögl, *Chem. Rev.*, 2015, **115**, 2818–2882.
- A. K. Datye, *J. Catal.*, 2003, **216**, 144–154.
- J.-D. Grunwaldt, J. B. Wagner and R. E. Dunin-Borkowski, *ChemCatChem*, 2013, **5**, 62–80.
- S. W. Chee, T. Lunkenbein, R. Schlögl and B. Roldán Cuenya, *Chem. Rev.*, 2023, **123**, 13374–13418.
- J. M. Thomas, C. Ducati, R. Leary and P. A. Midgley, *ChemCatChem*, 2013, **5**, 2560–2579.
- J. Qu, M. Sui and R. Li, *iScience*, 2023, **26**, 107072.
- B. He, Y. Zhang, X. Liu and L. Chen, *ChemCatChem*, 2020, **12**, 1853–1872.
- M. Newville, *J. Phys.: Conf. Ser.*, 2013, **430**, 012007.
- M. J. Piotrowski, C. G. Ungureanu, P. Tereshchuk, K. E. A. Batista, A. S. Chaves, D. Guedes-Sobrinho and J. L. F. Da Silva, *J. Phys. Chem. C*, 2016, **120**, 28844–28856.
- P. Giannozzi, S. Baroni, N. Bonini, M. Calandra, R. Car, C. Cavazzoni, D. Ceresoli, G. L. Chiarotti, M. Cococcioni, I. Dabo, A. Dal Corso, S. de Gironcoli, S. Fabris, G. Fratesi, R. Gebauer, U. Gerstmann, C. Gougoussis, A. Kokalj, M. Lazzeri, L. Martin-Samos, N. Marzari, F. Mauri, R. Mazzarello, S. Paolini, A. Pasquarello, L. Paulatto, C. Sbraccia, S. Scandolo, G. Sclauzero, A. P. Seitsonen, A. Smogunov, P. Umari and R. M. Wentzcovitch, *J. Phys.: Condens. Matter*, 2009, **21**, 395502.
- P. E. Blöchl, *Phys. Rev. B*, 1994, **50**, 17953–17979.
- G. Kresse and D. Joubert, *Phys. Rev. B*, 1999, **59**, 1758–1775.
- J. P. Perdew, K. Burke and M. Ernzerhof, *Phys. Rev. Lett.*, 1996, **77**, 3865–3868.
- J. Madsen and T. Susi, *Open Research Europe*, 2021, **1**, 24.
- T. Matsuo, Y. Yoshikawa and T. Aoshima, Mitsubishi Chemical corporation Pat. JP7111093B2, 2022.
- J. Zhao, L. Yang, J. A. McLeod and L. Liu, *Sci Rep*, 2015, **5**, 17779.
- A. Genc, J. Marlowe, A. Jalil, D. Belzberg, L. Kovarik and P. Christzopher, *Ultramicroscopy*, 2025, **271**, 114116.
- T. Siegrist, F. Hulliger and W. Petter, *Journal of the Less Common Metals*, 1983, **90**, 143–151.
- A. Rabus and E. Mun, *Phys. Rev. Mater.*, 2019, **3**, 013404.
- S. Gražulis, A. Daškevič, A. Merkys, D. Chateigner, L. Lutterotti, M. Quirós, N. R. Serebryanaya, P. Moeck, R. T. Downs and A. Le Bail, *Nucleic Acids Res*, 2012, **40**, D420–D427.
- T. Rapps, R. Ahlrichs, E. Waldt, M. M. Kappes and D. Schooss, *Angew. Chem. Int. Ed.*, 2013, **52**, 6102–6105.
- S. J. Pennycook and D. E. Jesson, *Ultramicroscopy*, 1991, **37**, 14–38.
- P. D. Nellist and S. J. Pennycook, *Ultramicroscopy*, 1999, **78**, 111–124.
- R. F. Loane, P. Xu and J. Silcox, *Acta Crystallogr A Found Crystallogr*, 1991, **47**, 267–278.



View Article Online
DOI: 10.1039/D5NR05414A

The data supporting this article have been included as part of the Supplementary Information. Supplementary information includes figures and tables for material characterization.

